




Article

High Precision Sinusoidal Position Tracking of a Voice-Coil Linear Servomotor Using Resonant Control

Rached Dhaouadi ^{*,†} , Mohannad Takroui [†]  and Ishaq Hafez [†] 

College of Engineering, American University of Sharjah, Sharjah 26666, United Arab Emirates

* Correspondence: rdhaouadi@aus.edu

† These authors contributed equally to this work.

Abstract: This paper presents a new sinusoidal position-tracking control scheme with a resonant controller for linear motor drive systems. The sinusoidal tracking controller is designed without any added algorithm for system identification and requires only approximate values of the mechanical parameters. Therefore, the controller is simple and robust to parameter variations. The proposed sinusoidal tracking resonant-based controller (STRC) is designed to track reference positions using a cascade control structure with an inner current/force control with hysteresis current control followed by a speed control loop with a resonant controller, and an outer position loop with a proportional and velocity-feedforward controller. The stability of the cascade feedback scheme and its parameter tuning are analyzed using the Routh–Hurwitz criterion. The performance of the proposed control scheme is validated using simulations and experiments on a voice-coil linear stage. The proposed STRC strategy is characterized by ease of implementation and shows excellent performance with fast response and high accuracy at different frequencies with a maximum error of 0.58% at 0.25 Hz.

Keywords: cascade control; linear servomotor; nonlinear friction; resonant controller; sinusoidal tracking; voice-coil motor



Citation: Dhaouadi, R.; Takroui, M.; Hafez, I. High Precision Sinusoidal Position Tracking of a Voice-Coil Linear Servomotor Using Resonant Control. *Electronics* **2023**, *12*, 977. <https://doi.org/10.3390/electronics12040977>

Academic Editors: Truong Quang Dinh, Junjie Chong, Adolfo Senatore, James Marco and Andrew McGordon

Received: 11 January 2023

Revised: 5 February 2023

Accepted: 10 February 2023

Published: 15 February 2023



Copyright: © 2023 by the authors. Licensee MDPI, Basel, Switzerland. This article is an open access article distributed under the terms and conditions of the Creative Commons Attribution (CC BY) license (<https://creativecommons.org/licenses/by/4.0/>).

1. Introduction

The motion control industry requires high-performance servomotor drives with linear torque or force control as well as high acceleration and frequency actuation. Voice-coil actuators (VCAs) are therefore ideal for this industry primarily due to their special structure, which offers a high amount of power per unit of volume, quiet operation, and smooth motion without backlash. Additionally, VCAs are fairly inexpensive compared to other linear actuators and are simpler to operate and control, making them advantageous for many motion-control applications [1–5]. The rotary VCA is, for example, commonly used in hard-disk drives to position the read/write head over the disk side [1,2]. On the other hand, linear VCAs are used for low-cost ultrasound scanners or in optical disk drives for the radial positioning of the objective lens [4,5]. The use of VCA in fast-steering mirrors is described in [6]. These mirrors require precise positioning to correct images captured by satellites. This is achieved using magnetic suspension and VCAs for low friction and responsive movement. The authors of [7] propose a method for real-time monitoring and compensation of motion coupling in a UAV multi-gimbal electro-optical pod using ultrasonic motors and VCAs, resulting in improved stability compared to traditional methods. The authors of [8] present a design of a 4-DOF VCA aimed at reducing laser geometrical fluctuations in the fast-steering mirror laser compensation system. Furthermore, [9] proposes a novel 3-DOF spherical VCA to address issues such as reduced efficiency, volume, response speed, and positioning accuracy compared to using multiple 1-DOF motors.

Although linear VCAs display low friction as a characteristic, their inherent nonlinearity can impact the performance of their positioning system when additional nonlinear friction is involved. Moreover, in most servomechanisms, a moving stage is always coupled

to the VCA through a linear bearing system. Additional sensors are also integrated for position feedback. This adds to the complexity of the overall system assembly. The integration of multiple discrete components will therefore be crucial, as it affects the reliability and the overall performance of the drive system.

In a linear servomechanism, there are two classes of friction, the first being static (between two surfaces not in relative motion) and the second being dynamic. The conventional method to represent static friction is a constant Coulomb friction force represented by a signum function that depends on the velocity direction. The disadvantage of this model is that friction is undefined at the velocity zero-crossing. Many improved models have been suggested in the literature to overcome this problem. This includes, for example, the Karnopp model and the Armstrong model [10]. More complex dynamic models have also been introduced to describe the dynamic behavior of friction such as the Stribeck effect and stick-slip limit cycles [11–13].

Force ripple due to cogging is another known disturbance force within linear drives. This is in addition to friction and reluctance forces [11]. Force ripple is usually described as a sinusoidal function of load position and is far more complex in shape as a result of variations in magnet dimensions in reality. This therein adds to the complexity of developing control algorithms that estimate and compensate for friction and force ripple. The problem of tracking sinusoidal and periodic disturbances and their cancellation has been addressed in many applications such as CD players and disk drives. The adopted technique known as “repetitive control” is usually used successfully to cancel such disturbances [14,15].

In the literature, researchers usually adopt frequency response or time response analysis for determination of mechanical as well as frictional parameters. There are various published models for the modeling and identification of friction [16–18], each carrying both advantages and disadvantages. Models are proposed based on physical insights, with some reporting extensive physical modeling yielding fixed structures accompanied by parameters of uncertain and unknown numerical values.

Friction compensation can be achieved by following two general techniques. The first approach relies on the determination of an accurate dynamic model of friction combined with its parameters’ identification procedure. This model is next combined with the motor drive model to design the adequate friction compensation scheme [2,11,12]. On the other hand, the second approach does not need to establish any friction model and treats friction as a system disturbance. Robust and adaptive control structures are then designed and optimized to counteract the disturbance effects [11–13,19,20].

Several researchers also propose adaptive disturbance rejection control (ADRC) for friction and disturbance compensation. ADRC was developed by modeling all the unknown dynamics and external disturbances to the given system as a one-equivalent disturbance. This total disturbance is next estimated by an extended-state observer in real time, and then used by the control law for disturbance rejection [21–25]. In [21], the authors proposed a nonlinear position-tracking controller with a disturbance observer to trace the required position despite a manifested disturbance in electrohydraulic actuators. The nonlinear controller has a cascade structure with an inner-load pressure control loop and an outer position loop with a backstepping controller. In [22], the authors propose an ADRC-based control method with a single position feedback loop to improve the dynamic performance of the voice-coil motor. The proposed control scheme is validated by simulation and experiments and is shown to perform much better than traditional cascaded-loop PI controllers. In [23], the authors use ADRC for the speed control of a VCM servo-drive system. The controller parameters were tuned using a neural network with a radial basis function. The proposed algorithm was compared to a PID controller to highlight the achieved high performance. In [24], an improved ADRC controller is proposed. Simulation results show that the improved ADRC has a fast response, high precision, and strong robustness to disturbances. Another improved method based on sliding-mode ADRC is presented in [25]. Internal and external perturbations are estimated, along with position and velocity, and used for disturbance compensation.

Moreover, resonant controllers have been commonly used for sinusoidal tracking in power systems, active power filters, and active power factor correction, among other applications [26–34]. Nevertheless, a stable and robust realization of a perfect resonant controller is difficult to accomplish practically. Accordingly, quasi-resonant controllers are typically utilized in practical applications. Model predictive control has also been used for sinusoidal reference tracking in combination with resonant control [35,36].

All these approaches have their respective advantages addressing some specific problems for the studied systems. However, they are model-based control techniques and require accurate knowledge of the system or an additional identification algorithm for identifying model parameters. In addition, there is hardly one method which can tackle the precise signal tracking issue for a wide frequency range, especially at low frequencies where the influence of nonlinear disturbances such as static and Coulomb friction are dominant.

Model reference adaptive control (MRAC) has also been used in the literature to control servo-drive systems without prior knowledge about the system parameters [37–39]. MRAC is a control method that uses a reference model to generate a desired response, and the control action is adjusted in real time based on the difference between the actual response and the desired response. The parameters of the reference model are updated using adaptive algorithms that continuously learn the system dynamics based on the plant's response. This allows MRAC to handle changes in plant dynamics over time, making it a powerful tool for controlling systems without prior knowledge of their parameters. MRAC can result in improved control performance compared to traditional controllers and is well-suited for applications in which the system parameters are difficult or expensive to measure.

The suggested model-free approach provides many advantages over model-based methods, particularly the ease of implementation across various systems. The model-free approach also relieves the user of the requirement to be an expert on the model, unlike the extensive friction models that require a time-consuming identification-based modeling phase for each run. Furthermore, linear VCA stages are characterized by position-dependent friction, a feature that is not simple to include in currently available friction models.

The main contribution of this paper is the design and implementation of a sinusoidal position-tracking control scheme with a new resonant controller for use in linear motor drive systems. This paper follows the same approach used in model-based controls, where all the nonlinearities such as friction are represented as external system disturbances. The sinusoidal resonant tracking controller is designed without any added algorithm for system identification and requires only approximate values of the mechanical parameters. Therefore, the controller is simple and robust to parameter variations. The aim is to enhance the accuracy of positioning by rectifying the nonlinear behavior of velocity during zero-crossing caused by Coulomb and static friction.

The proposed sinusoidal tracking resonant-based controller (STRC) shows excellent dynamic performance with fast transient response, high accuracy, and good disturbance rejection compared to existing control methods. A new resonant controller combined with an optimal cascade control structure is proposed. The corresponding parameter-tuning method is characterized by ease of implementation without the need for the exact knowledge of the mechanical system parameters. The performance of the proposed method is validated via simulations and experiments.

The paper is organized as follows: Section 2 outlines the mathematical model of the linear voice-coil actuator. Section 3 presents the proposed STRC control scheme. Section 4 introduces the ADRC method. Section 5 discusses the experimental setup and results. Finally, Section 6 concludes the paper with a summary of the conclusions.

2. System Modeling

The linear servomotor used in this study is a linear voice coil-actuator (VCA), as illustrated in Figure 1. The VCA is an electromechanical device, which can be described by the following equations of motion [40]:

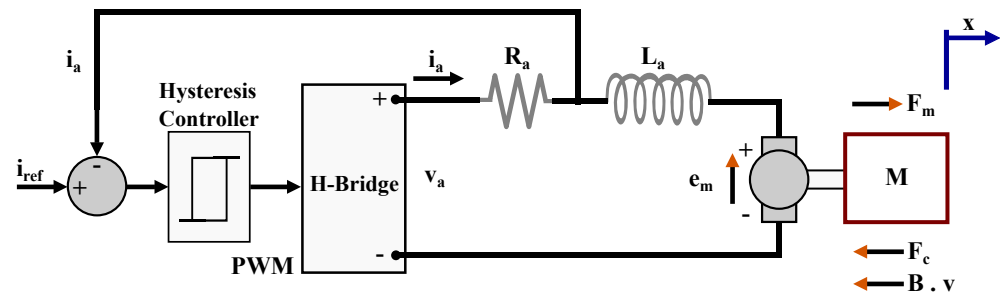


Figure 1. Equivalent model of a voice-coil DC motor.

$$L_a \frac{di_a}{dt} = V_a - R_a i_a - e_m, \quad (1)$$

$$e_m = K_b v, \quad (2)$$

$$M \frac{dv}{dt} = F_m - F_c \text{sign}(v) - Bv, \quad (3)$$

$$v = \frac{dx}{dt}, \quad (4)$$

$$F_m = K_f i_a, \quad (5)$$

where v and i_a are the motor linear velocity and coil current; R_a and L_a , are the resistance and inductance of the coil; V_a , e_m , and K_b are the applied voltage, back electromotive force (EMF), and back EMF constant; M and B are the mass and viscous friction coefficient; F_m and K_f are the actuator force and force constant; and F_c is the Coulomb friction force.

The linear VCM has a cascade control structure with an internal hysteresis current-controller. The hysteresis current control loop allows for decoupling of the electrical dynamics from the mechanical dynamics. When the current hysteresis band is sufficiently small, the current/force control loop can be represented by an equivalent first order system with a transfer function given by:

$$G_c(s) = \frac{F_m(s)}{I_{ref}(s)} = \frac{K_f}{1 + \tau_c s}, \quad (6)$$

where τ_c is the equivalent time constant of the current control loop in (sec). The equivalent motor transfer function is therefore reduced to:

$$G_m(s) = \frac{v(s)}{F(s)} = \frac{K_m}{1 + \tau_m s}, \quad (7)$$

where

$$K_m = \frac{1}{B}, \quad (8)$$

$$\tau_m = \frac{M}{B}. \quad (9)$$

3. Controller Design

The proposed STRC controller is designed to track the reference position using a cascade control structure with an inner current/force control with hysteresis current control followed by a speed control loop with a resonant controller, and an outer position loop with a proportional and velocity-feedforward controller. The proposed control scheme is illustrated in Figure 2. The linear motor drive system is represented by its equivalent block diagram with the internal current control loop. The main disturbance consists of Coulomb and sticktion frictions. Any additional load torque is represented as a disturbance to the linear system.

$$G_{clv}(s) = \frac{K(s + \alpha)^2}{den_{clv}}, \quad (16)$$

where

$$den_{clv} = \tau_c \tau_m s^4 + (\tau_c + \tau_m) s^3 + (1 + \omega_0^2 \tau_c \tau_m + K) s^2 + (\omega_0^2 (\tau_c + \tau_m) + 2\alpha K) s + K\alpha^2 + \omega_0^2. \quad (17)$$

The outer position loop includes a proportional controller and a velocity-feedforward controller. The position controller is given by:

$$G_p(s) = K_p. \quad (18)$$

The open loop transfer function for the whole system is given by:

$$G_{olp}(s) = G_{clv}(s) \cdot \frac{K_p}{s} = \frac{K_p K (s + \alpha)^2}{s den_{clv}}. \quad (19)$$

The closed loop transfer function for the system is given by:

$$G_{clp}(s) = \frac{K_p K (s + \alpha)^2}{s den_{clv} + K_p K (s + \alpha)^2}. \quad (20)$$

The overall control scheme parameterization makes the STRC controller a function of three parameters, namely the position loop-gain K_p , the resonant controller gain K_v , and the zero α . The flexible range of these variables greatly simplifies the tuning process as described in the following section.

3.1. Velocity Controller Design

Velocity controller gains are designed by deriving the upper and lower bounds using the stability analysis of the velocity control with the Routh–Hurwitz criteria [41]. Given the denominator of the closed loop transfer function in Equation (16), the Routh table is derived as shown in Table 1.

Table 1. Routh table for the velocity control loop.

s^4	$\tau_c \tau_m$	$1 + \omega_0^2 \tau_c \tau_m + K$	$K\alpha^2 + \omega_0^2$
s^3	$\tau_c + \tau_m$	$\omega_0^2 (\tau_c + \tau_m) + 2\alpha K$	0
s^2	A_v	B_v	
s^1	C_v	0	
s^0	$D_v = B_v$	0	

To simplify the calculations, let:

$$\tau_{sum} = \tau_m + \tau_c, \quad (21)$$

$$\tau_{prd} = \tau_m \times \tau_c, \quad (22)$$

$$\frac{1}{\tau_{eq}} = \frac{1}{\tau_m} + \frac{1}{\tau_c} = \frac{\tau_{sum}}{\tau_{prd}}. \quad (23)$$

Then, the terms A_v , B_v , C_v , and D_v in Table 1 can be found to be:

$$A_v = -2K \tau_{eq} \alpha + K + 1, \quad (24)$$

$$B_v = K\alpha^2 + \omega_0^2, \quad (25)$$

$$C_v = \frac{A_v (\omega_0^2 \tau_{sum} + 2\alpha K) - B_v \tau_{sum}}{A_v}, \quad (26)$$

$$D_v = B_v = K \alpha^2 + w_0^2. \quad (27)$$

For the system to be stable, the terms A_v , C_v , and D_v must be greater than zero. For condition $A_v > 0$, α can be found as:

$$\alpha < \frac{1}{2 \tau_{eq}} \left(\frac{1}{K} + 1 \right). \quad (28)$$

A conservative boundary condition for α can be used which allows for α to be chosen independently of K_v as follows:

$$\alpha < \frac{1}{2 \tau_{eq}}. \quad (29)$$

Rearranging the condition, $C_v > 0$ leads to the boundary conditions:

$$K_v > 0, \quad (30)$$

and

$$K_v > \frac{1}{2K_f K_m} \left[\frac{2 - \tau_{sum} \alpha}{2 \alpha \tau_{eq} - 1} - \frac{w_0^2 \tau_{sum}}{\alpha} \right]. \quad (31)$$

A conservative condition for K_v can be used which allows for K_v to be chosen independently of ω_0 as follows:

$$K_v > \frac{1}{2K_f K_m} \left[\frac{2 - \tau_{sum} \alpha}{2 \alpha \tau_{eq} - 1} \right]. \quad (32)$$

On the other hand, the condition $D_v > 0$ is always satisfied when $K_v > 0$.

The resonant controller-tuning procedure can be summarized as follows:

- The variable α is selected to satisfy the condition given in (29).
- The gain K_v is selected to satisfy the condition given in (32).
- The above two conditions can be achieved without the exact knowledge of the mechanical system parameters K_f , K_m , τ_c , and τ_m . Only approximate values of these parameters are needed to select the appropriate controller variables and assure system stability.
- The current control loop time constant τ_c is usually very small compared to the mechanical time constant τ_m . Therefore, $\frac{1}{\tau_{eq}} \simeq \frac{1}{\tau_c}$. This gives more flexibility in the selection on the variable α .

Figure 3 shows the root locus plot for the velocity loop as a function of the gain K_v for $\alpha = 100$. It can be shown that, for different values of α , the system is always stable if K_v is bigger than the lower bound set by Equation (32). This lower bound corresponds to the crossing of the imaginary axis on the root locus as K_v is increased. Therefore, as the gain K_v is increased, a higher stability margin is achieved.

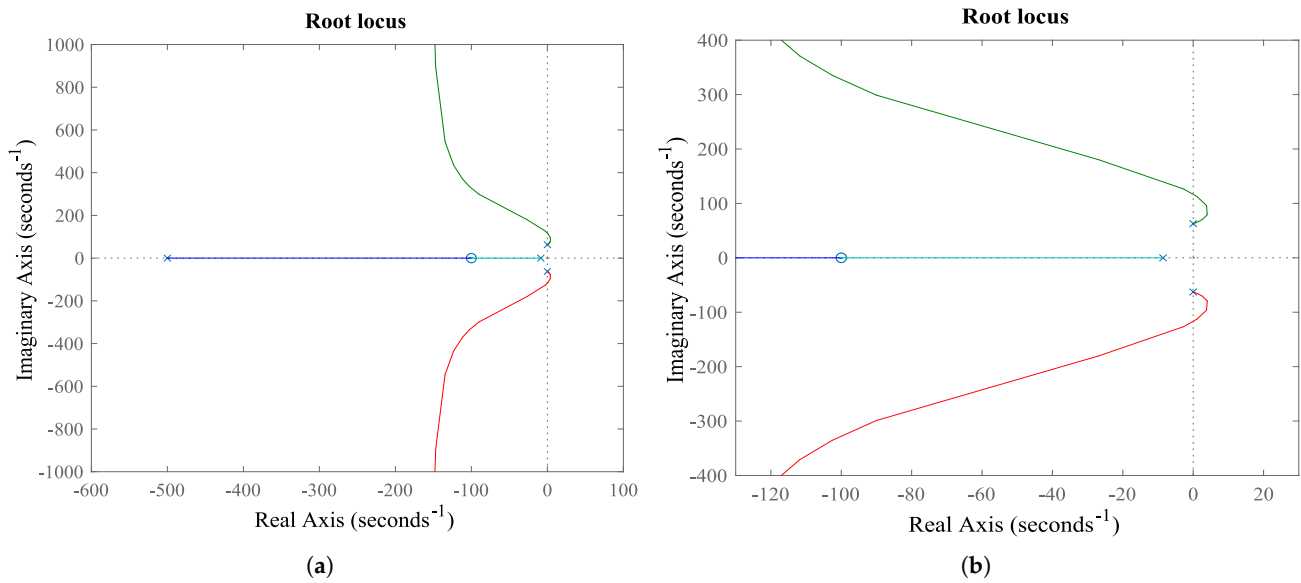


Figure 3. (a) Root locus plot for the internal velocity loop as a function of the gain K_v ; (b) zoomed view of the root locus. For small values of K_v , the closed-loop system poles move to the right-hand s-plane. To guarantee stability, K_v should be increased beyond a lower-bound value.

3.2. Position Controller Design

The position controller gain is designed by deriving the upper bound using the closed-loop transfer function given by (20) along with the Routh–Hurwitz stability criteria. The Routh table is shown in Table 2.

Table 2. Routh table for the position-control loop.

s^5	$\tau_c \tau_m$	$1 + \omega_0^2 \tau_c \tau_m + K$	$(2\alpha K_p + \alpha^2)K + \omega_0^2$
s^4	$\tau_c + \tau_m$	$\omega_0^2(\tau_c + \tau_m) + (K_p + 2\alpha)K$	$\alpha^2 K_p K$
s^3	A_p	B_p	0
s^2	C_p	D_p	
s^1	E_p	0	
s^0	$F_p = D_p$	0	

The terms A_p , B_p , C_p , D_p , E_p , and F_p in Table 2 can be found to be:

$$A_p = K - K \tau_{eq} (2\alpha + K_p) + 1, \quad (33)$$

$$B_p = \omega_0^2 + K \alpha^2 + K_p K \alpha (2 - \alpha \tau_{eq}), \quad (34)$$

$$C_p = \frac{A_p(\omega_0^2 \tau_{sum} + (K_p + 2\alpha)K) - B_p \tau_{sum}}{A_p}, \quad (35)$$

$$D_p = K \alpha^2 K_p, \quad (36)$$

$$E_p = \frac{B_p C_p - A_p D_p}{C_p}, \quad (37)$$

$$F_p = D_p = K \alpha^2 K_p. \quad (38)$$

For the system to be stable, the gain K_p should satisfy the following four conditions. The variables K_v and α are assumed to be given and have been selected based on the velocity-loop stability criteria.

$$\begin{aligned}
A_p &> 0, \\
C_p &> 0, \\
E_p &> 0, \\
F_p &> 0.
\end{aligned} \tag{39}$$

The A_p condition is:

$$(-K \tau_{eq}) K_p + K - 2 K \alpha \tau_{eq} + 1 > 0, \tag{40}$$

$$K_p < \frac{K - 2 K \alpha \tau_{eq} + 1}{K \tau_{eq}}. \tag{41}$$

The F_p condition is:

$$K \alpha^2 K_p > 0, \tag{42}$$

$$K_p > 0. \tag{43}$$

The C_p condition is:

$$c_1 K_p^2 + c_2 K_p + c_3 > 0, \tag{44}$$

where

$$c_1 = -K \tau_{eq}, \tag{45}$$

$$c_2 = -(w_0^2 - \alpha^2) \tau_{prd} - 4 \alpha K \tau_{eq} - 2 \alpha \tau_{sum} + K + 1, \tag{46}$$

$$c_3 = -(\alpha^2 - w_0^2) \tau_{sum} - 2 \alpha w_0^2 \tau_{prd} - 4 \alpha^2 K \tau_{eq} + 2 \alpha (1 + K). \tag{47}$$

Equation (44) can be solved by calculating the roots K_{p1} and K_{p2} of the equation and setting K_p to be between the roots $K_{p1} < K_p < K_{p2}$.

The E_p condition results in a third order inequality for the gain K_p :

$$e_1 K_p^3 + e_2 K_p^2 + e_3 K_p + e_4 > 0, \tag{48}$$

where

$$e_1 = -2 K^3 \alpha \tau_{eq}, \tag{49}$$

$$\begin{aligned}
e_2 = & K^2 (2 \alpha + 2 K \alpha + \alpha^2 \tau_{eq} - 4 \alpha^2 \tau_{sum} - \tau_{eq} w_0^2 + 4 \alpha^3 \tau_{eq} \tau_{sum} - \alpha^4 \tau_{eq}^2 \tau_{sum} \\
& - 8 K \alpha^2 \tau_{eq} + \alpha^2 \tau_{eq}^2 \tau_{sum} w_0^2 - \sigma_2),
\end{aligned} \tag{50}$$

$$\begin{aligned}
e_3 = & K \sigma_1 (-\tau_{eq} \tau_{sum} w_0^2 + K - 4 K \alpha \tau_{eq} + 1) - K \alpha^2 \sigma_3^2 + 2 K \alpha \tau_{sum} (\alpha \tau_{eq} - 2) \sigma_1 \\
& - K \alpha (\tau_{sum} w_0^2 + 2 K \alpha) (\alpha \tau_{eq} - 2) \sigma_3,
\end{aligned} \tag{51}$$

$$e_4 = K \sigma_1 (2 \alpha + 2 K \alpha - \alpha^2 \tau_{sum} + w_0^2 \tau_{sum} - 4 K \alpha^2 \tau_{eq} - \sigma_2), \tag{52}$$

and

$$\begin{aligned}
\sigma_1 &= K \alpha^2 + w_0^2, \\
\sigma_2 &= 2 \alpha \tau_{eq} \tau_{sum} w_0^2,
\end{aligned} \tag{53}$$

$$\sigma_3 = K - 2 K \alpha \tau_{eq} + 1.$$

Equation (48) can be solved graphically using the Matlab Symbolic Toolbox to find the upper bound on K_p for given values of K_v , α , and ω_0 . The Matlab Symbolic Toolbox utilized in our work was version 2021b provided in the MATLAB software suite developed by © MathWorks, Inc. (Natick, MA, USA). The Matlab Symbolic Toolbox is a tool in MATLAB for symbolic math computations, including solving mathematical equations and performing calculus operations.

Figure 4 shows the root locus plot for the outer position loop as a function of the gain K_p for $K_v = 10$, $\alpha = 100$, and $f_0 = 10\text{Hz}$. Figure 5 shows the upper boundary curves obtained from the conditions in (39). It can be observed that boundary condition $E_p > 0$ is the dominant curve to limit the value of K_p . For a large value of the gain K_v , the curves for $E_p > 0$ and $A_p > 0$ get close to each other. It was also observed that the variable ω_0 has little effect on the second and third boundary conditions. Since the analytical expression of condition 1 ($A_p > 0$) is relatively simple, it can be used to find the upper boundary condition for K_p when K_v is relatively large.

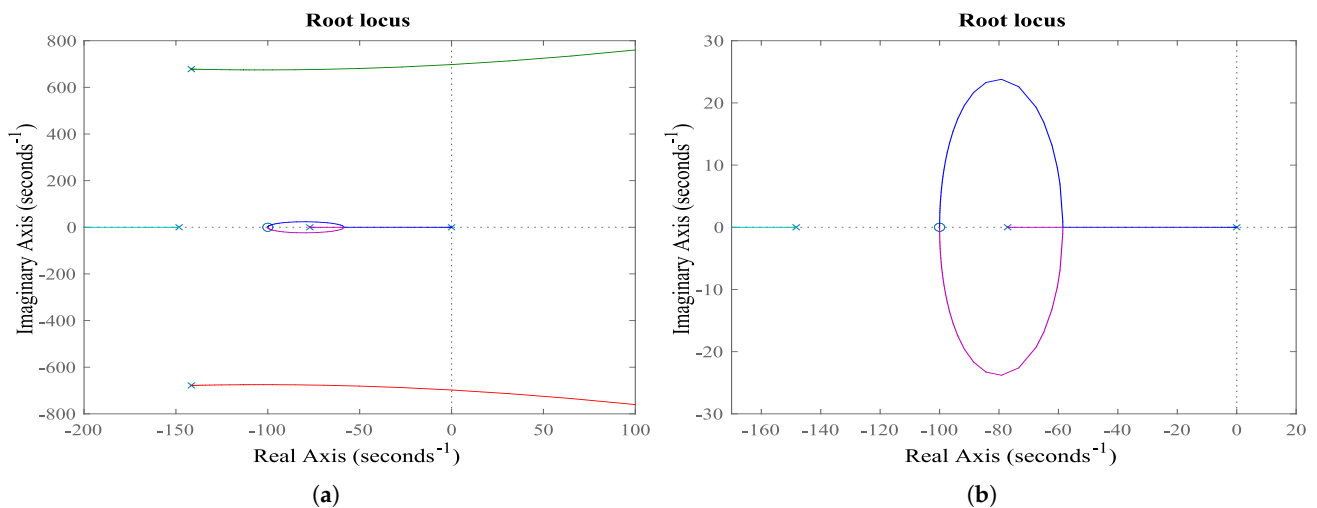


Figure 4. (a) Root locus plot for the outer position loop as a function of the gain K_p ; (b) zoomed view of the root locus. The system is stable as the gain K_p is increased up to the upper boundary value given by (39).

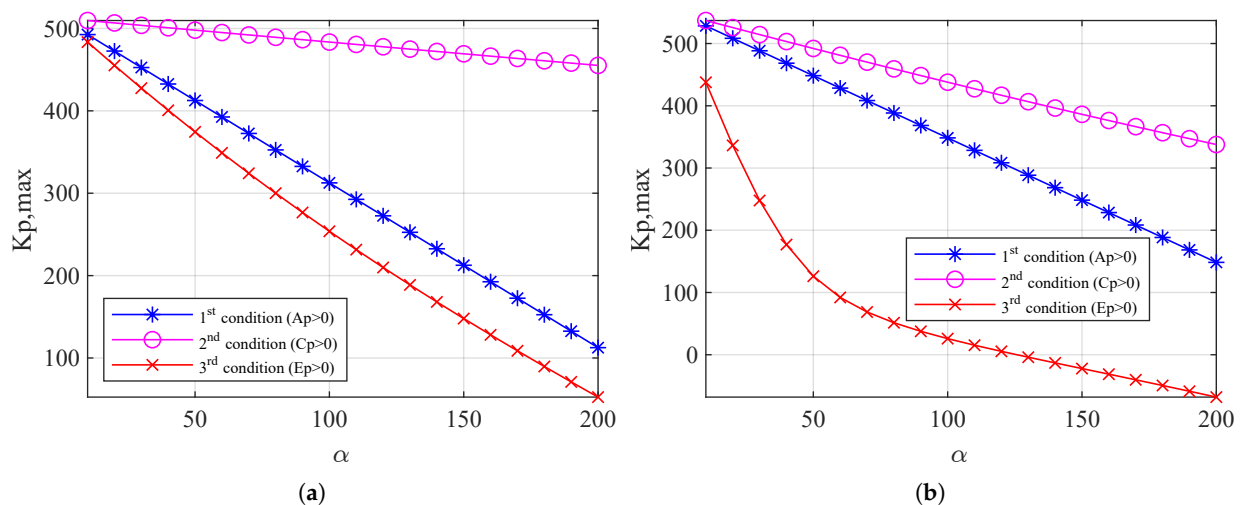


Figure 5. Maximum boundary conditions for the gain K_p as a function of α for $f_0 = 1.0\text{ Hz}$ and (a) $K_v = 100$, (b) $K_v = 10$.

4. Active Disturbance Rejection Controller

The active disturbance rejection controller (ADRC) is one of the highly effective controllers that have been shown to be superior to classical PID controllers. The ADRC was first proposed by Prof. Han Jing-Qing in 1995, and it has been used in various applications in much of the relevant literature [23,42].

The ADRC is a nonlinear controller with an error-driven scheme that can effectively control a dynamic system without requiring an accurate model [42]. Figure 6 shows the configuration of the controller, consisting of three main components: a tracking profile generator (TPG), a nonlinear weighted sum (NWS), and an extended state observer (ESO).

In reference tracking systems, it is desired to design reference signal $x_{ref}(t)$ in a physically feasible way to minimize tracking and initial errors. The TPG, introduced by Han, is a reference generator used in ADRC to smooth sudden changes in the reference signal. It helps to track the output of the TPG during sudden overshoot, reducing unexpected overshoot and rapidity of the PID controller while preserving the system response speed [42]. The TPG can be designed in the discrete-time domain as follows:

$$\begin{aligned} r_1(t+1) &= r_1(t) + h r_2(t), \\ r_2(t+1) &= r_2(t) + h fhan(r_1(t) - x_{ref}, r_2(t), \kappa, h_0), \end{aligned} \quad (54)$$

where $r_1(t)$ is the control target, $r_2(t)$ is the derivative of the desired trajectory at t , and h is the sampling time. Han's function, $fhan(\cdot)$, represents Han's function with parameters κ , the tracking speed factor, and h_0 , the tracking filtering factor. κ controls the speed of transition and h_0 affects the smoothness of the output response [42,43]. The Han's function $fhan(\varepsilon_1, \varepsilon_2, \kappa, h_0)$ is defined as follows [42,43]:

$$d = \kappa h_0, \quad d_0 = h_0 d, \quad g = \varepsilon_1 + h_0 \varepsilon_2, \quad (55)$$

$$a_0 = \sqrt{d^2 + 8\kappa|g|}, \quad (56)$$

$$a = \begin{cases} \varepsilon_2(k) + \frac{g}{h_0}, & |g| < d_0 \\ \varepsilon_2(k) + \frac{\text{sign}(g)(a_0-d)}{2}, & |g| \geq d_0 \end{cases} \quad (57)$$

$$fhan = \begin{cases} \kappa \frac{a}{d}, & |a| \leq d \\ -\kappa \text{sgn}(a), & |a| > d \end{cases} \quad (58)$$

The parameters κ and h_0 are adjusted individually to match the desired tracking speed and smoothness of the system's output response, but there is no constructive technique for tuning them, as per [43]. The NWS uses a nonlinear function that relies on error signals to produce the control signal. It calculates state variable errors by taking the difference between the TPG output and ESO state variables. Then, the control signal $u(t)$ is derived, as per [43].

$$u(t) = \frac{-z_3(t) + \varphi_1 \text{fal}(e_1(t), \lambda_1, \psi_1) + \varphi_2 \text{fal}(e_2(t), \lambda_2, \psi_2)}{b_0}, \quad (59)$$

where $e_1 = r_1 - z_1$ and $e_2 = r_2 - z_2$, $b_0 = K_f/M$, φ_1 and φ_2 are controller gains, and $\lambda_1, \lambda_2, \psi_1$ and ψ_2 are the parameters of the function $\text{fal}(\cdot)$. Substituting (59) in (64), if the ESO is very accurate, the result of $F(y(t), u(t), d(t)) - z_3$ can be negligible. Therefore, (59) can be written as,

$$\ddot{y}(t) = \varphi_1 \text{fal}(e_1, \lambda_1, \psi_1) + \varphi_2 \text{fal}(e_2, \lambda_2, \psi_2). \quad (60)$$

The controller's tuning is simplified by setting $\varphi_1 = 3\omega_c^2$ and $\varphi_2 = 3\omega_c$, where ω_c is the closed-loop control bandwidth [24,25,43]. The larger ω_c is, the faster the response. Both ω_0 and ω_c are limited by hardware constraints, and ω_0 is commonly set to $3 \sim 5\omega_c$.

The ESO uses dynamic functions to estimate unmeasurable variables, such as errors and disturbances. It outputs 3 signals: $z_1(t)$ approximates $y(t)$, $z_2(t)$ approximates $y(t)'$, and $z_3(t)$ approximates disturbances. The control signal is adjusted based on the ESO estimates' accuracy. Equation (61) defines the observer design, and observer gains are tuned by ω_0 in Equation (63).

$$\begin{aligned} e(t) &= z_1(t) - y(t), \\ z_1(t+1) &= z_1(t) + h[z_2(t) - \chi_1 e(t)], \\ z_2(t+1) &= z_2(t) + h[z_3(t) - \chi_2 fal(e(t), \epsilon_1, \eta_1) + b u(t)], \\ z_3(t+1) &= z_3(t) - h[\chi_3 fal(e(t), \epsilon_2, \eta_2)], \end{aligned} \quad (61)$$

where χ_1 , χ_2 , and χ_3 are observer gains, and ϵ_1 , ϵ_2 , η_1 , and η_2 are parameters for the function $fal(\cdot)$ in Equation (62):

$$fal = \begin{cases} \frac{e}{\eta^{1-\epsilon}} & |e| \leq \eta \\ |e|^\epsilon \text{sign}(e), & |e| > \eta \end{cases}, \quad (62)$$

where ϵ is specified in the range $(0, 1)$ and η is a multiple of the sampling time h .

$$\begin{aligned}\chi_1 &= 3\omega_0, \\ \chi_2 &= 3\omega_0^2, \\ \chi_3 &= \omega_0^3.\end{aligned}\tag{63}$$

A greater value for ω_0 means the observer runs faster.

As seen in Figure 6, the ESO takes system output $y(t)$ and control signal $u(t)$ as inputs. It generates 3 signals: $z_1(t)$ approximates $y(t)$, $z_2(t)$ approximates $y(t)'$, and $z_3(t)$ approximates disturbances. The ADRC adjusts control based on the ESO's accuracy in estimating uncertainties, including model errors [24,42,43].

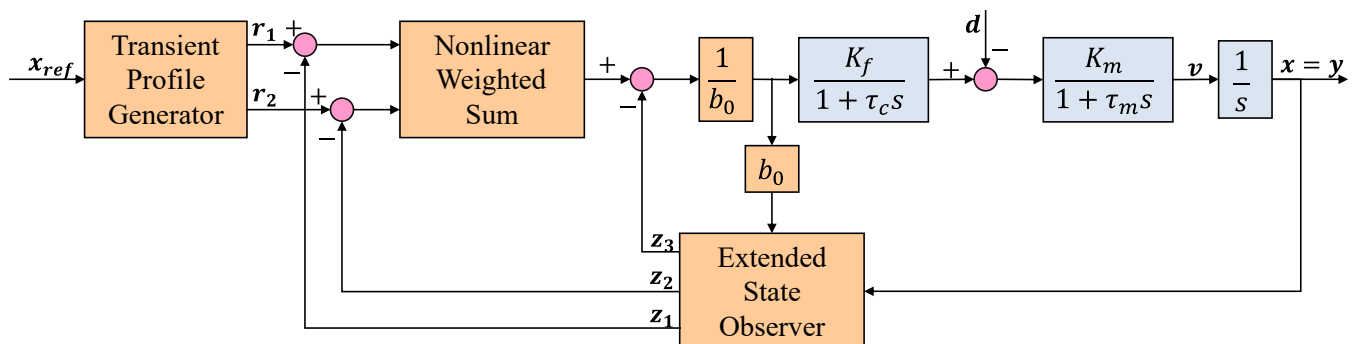


Figure 6. Block diagram of active disturbance rejection controller.

Consider a dynamic system represented by the following equation [23,42,43]:

$$\ddot{y}(t) = F(y(t), u(t), d(t)) + b_0 u(t), \quad (64)$$

where $y(t)$ is the system's output, $u(t)$ is the control signal, $d(t)$ is an external disturbance, and b_0 is an approximate estimate of the control signal gain. $F(t)$ is the generalized disturbance that is estimated in real time and compensated by the control signal, $u(t)$ [44].

Let $x_1(t) = x = y(t)$, $x_2(t) = \dot{x}_1(t)$ and $x_3(t) = F(t)$. Assuming the unknown function $F(t)$ is differentiable, then $\delta(t) = \dot{F}(t)$, and the system can be expressed in the state-space model as follows:

$$\begin{aligned} \dot{x}_1(t) &= x_2(t), \\ \dot{x}_2(t) &= x_3(t) + b_0 u(t), \\ \dot{x}_3(t) &= \delta(t), \end{aligned} \quad (65)$$

with the system state $x(t) = [x_1(t), x_2(t), x_3(t)]^T$.

For the voice-coil motor, the mechanical system equations with current control reduce to only Equations (3)–(5), which can be expressed as:

$$\frac{dv}{dt} = \frac{1}{M} (K_f i_a) - \frac{1}{M} F_c \operatorname{sign}(v) - \frac{B}{M} v. \quad (66)$$

If the Coulomb friction is considered as a disturbance d , Equation (66) can be written as:

$$\frac{dv}{dt} = \frac{K_f}{M} i_a - \frac{1}{M} d - \frac{B}{M} v. \quad (67)$$

Both viscous and Coulomb frictions can be combined as the generalized disturbance $F(y(t), u(t), d(t))$. Equation (66) can now be written as:

$$\frac{dv}{dt} = b_0 i_a + F(y(t), u(t), d(t)), \quad (68)$$

where

$$b_0 = \frac{K_f}{M}. \quad (69)$$

If the current control loop is assumed to be very fast, then:

$$i_a = i_{ref}. \quad (70)$$

5. Results and Discussion

5.1. Experimental Setup

The linear voice-coil DC motor VCDS-051- 089-01-13 from MotiCont is adopted for the experimental setup [45]. The linear stage has a 55.9 mm range of motion and a built-in incremental encoder with 500 pulse/inch resolution. Another high-resolution analog encoder is fitted to the moving stage to evaluate the linear position with a higher resolution of 0.078125 μm . The actuator force is controlled through a hysteresis current-controller, which is implemented in the dSPACE 1103 control board with a 10 μs sampling period. Figure 7 shows the different components of the VCM positioning system.

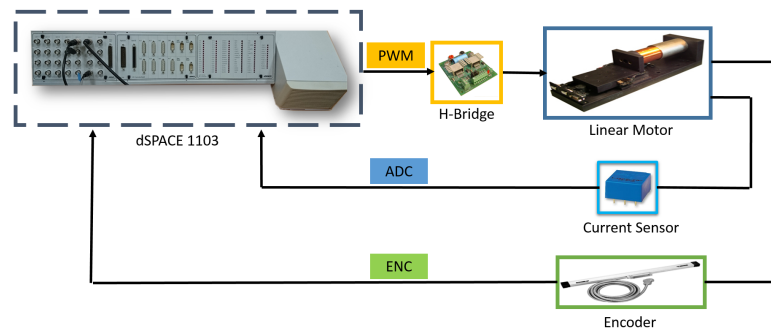


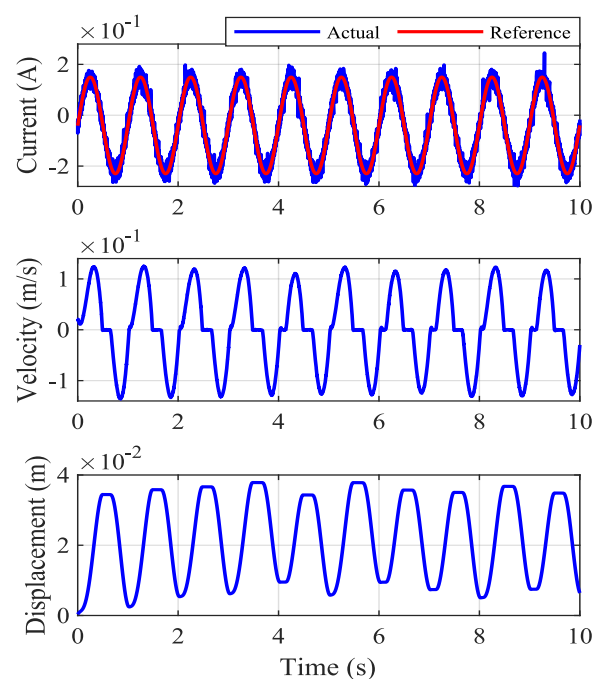
Figure 7. Signals interfaced to the dSPACE 1103 controller board along with their corresponding hardware components.

The VCM parameters (M , B , and F_c) are found using the parameter estimation toolbox in Matlab. The VCM is operated in current-control mode with a square-wave reference current signal, and the measured velocity is used for parameter identification. The equivalent time constant of the current control loop τ_c is found using Matlab by finding the first order transfer function of the digital hysteresis current-controller. The motor force constant K_f is given in the manufacturer datasheet. The nominal system parameters are listed in Table 3.

Table 3. Nominal parameters of the voice-coil motor.

Parameter	Value
M (Kg)	0.9232
B (N.s/m)	7.9124
F_c (N)	0.5035
K_f (N/A)	10.1
K_m (m/N.s)	0.1264
τ_m (s)	0.1167
τ_c (s)	0.002

Figure 8 shows the experimental results of the open-loop response to a sinusoidal reference current/force at 1 Hz. The results clearly show the highly nonlinear behavior of the VCM, which is mainly due to high nonlinear static and Coulomb friction. The velocity dead-zone during zero-crossing induces flat peaks in displacement and result in a highly distorted sinusoidal displacement curve.

**Figure 8.** Experimental results of the open-loop response to a sinusoidal reference current/force at 1.0 Hz.

5.2. STRC Response at Different Frequencies

Different experiments are next performed to test the closed-loop system and track sinusoidal references at different frequencies. The controller parameters are selected to satisfy the stability constraints derived in Section 3. To allow a smooth transient, the position and speed references are generated to start both from zero initial conditions as follows:

$$x_{ref}(t) = X_m [1 - \cos(\omega_0 t)], \quad (71)$$

$$v_{ref}(t) = \omega_0 X_m \sin(\omega_0 t). \quad (72)$$

Figures 9–11 show the motor current, speed, position reference, actual position, as well as the position error for three experimental tests with $f_0 = 1.0$ Hz, 0.5 Hz, and 0.25 Hz for $\alpha = 5$, $K_v = 20$, $K_p = 40$. The maximum error is about $1.81e^{-4}m$, which corresponds to 0.72% of the reference signal amplitude at 0.25Hz. The corresponding settling time is about 0.12 s, which is very small and much less than a quarter of a cycle. Increasing the gain K_p further within the maximum limit will lead to a shorter settling time.

Figure 12 shows the system response at 0.25 Hz with a different gain setting for α . The higher value of $\alpha = 50$ is within the design constraint given by (29) and gives a better system-tracking performance with a lower maximum error of about 0.58%. The position distortion due to friction is greatly reduced.

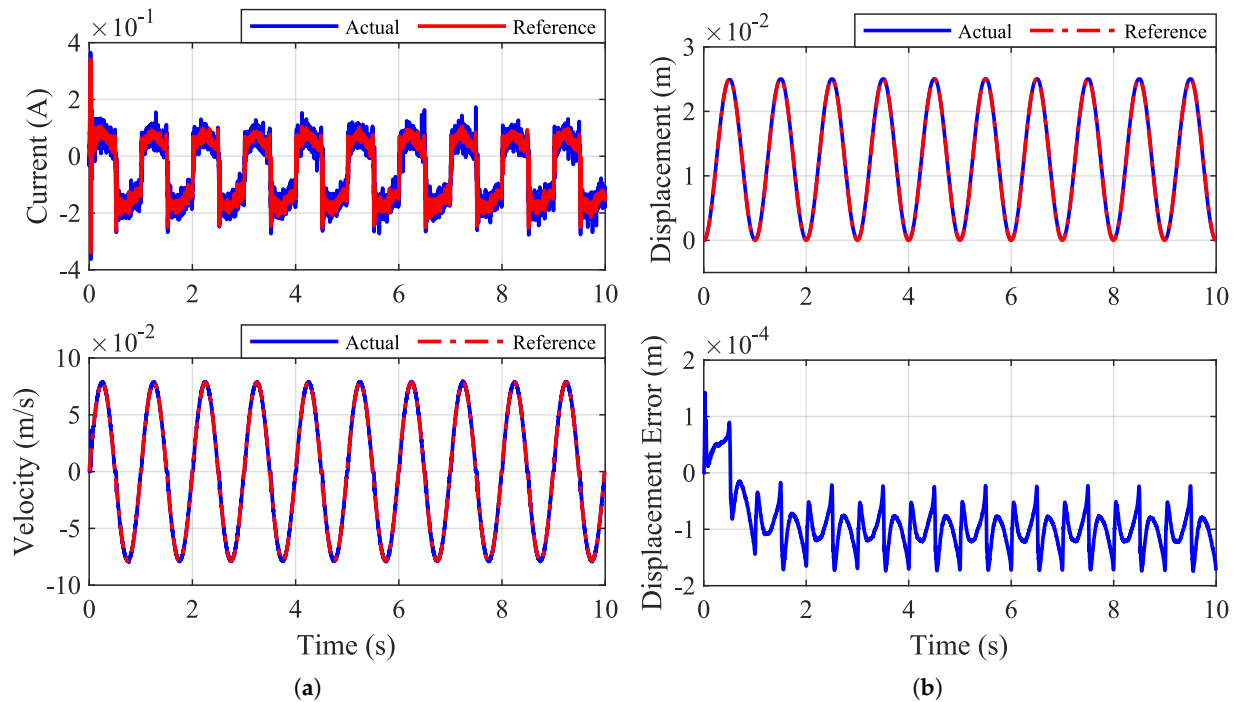


Figure 9. Experimental waveforms for sinusoidal position tracking at 1.0 Hz with $\alpha = 5$, $K_v = 20$, $K_p = 40$. (a) Current and velocity; (b) displacement and displacement error.

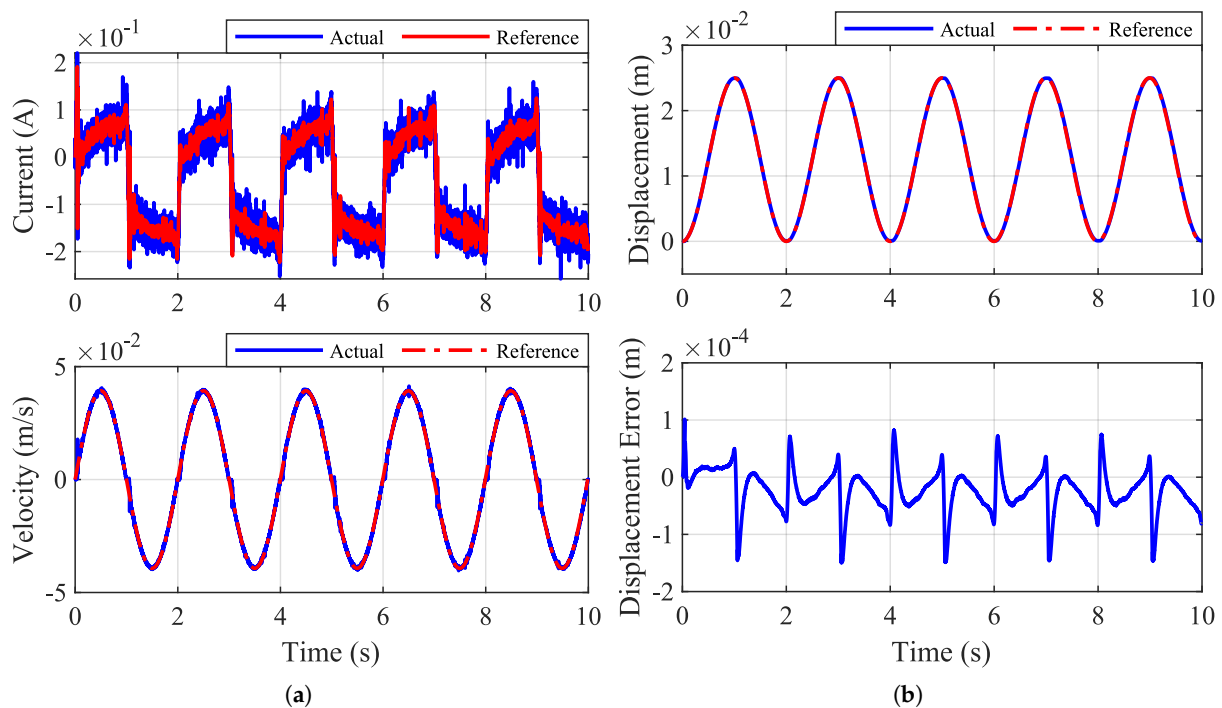


Figure 10. Experimental waveforms for sinusoidal position tracking at 0.5 Hz with $\alpha = 5$, $K_v = 20$, $K_p = 40$. (a) Current and velocity; (b) displacement and displacement error.

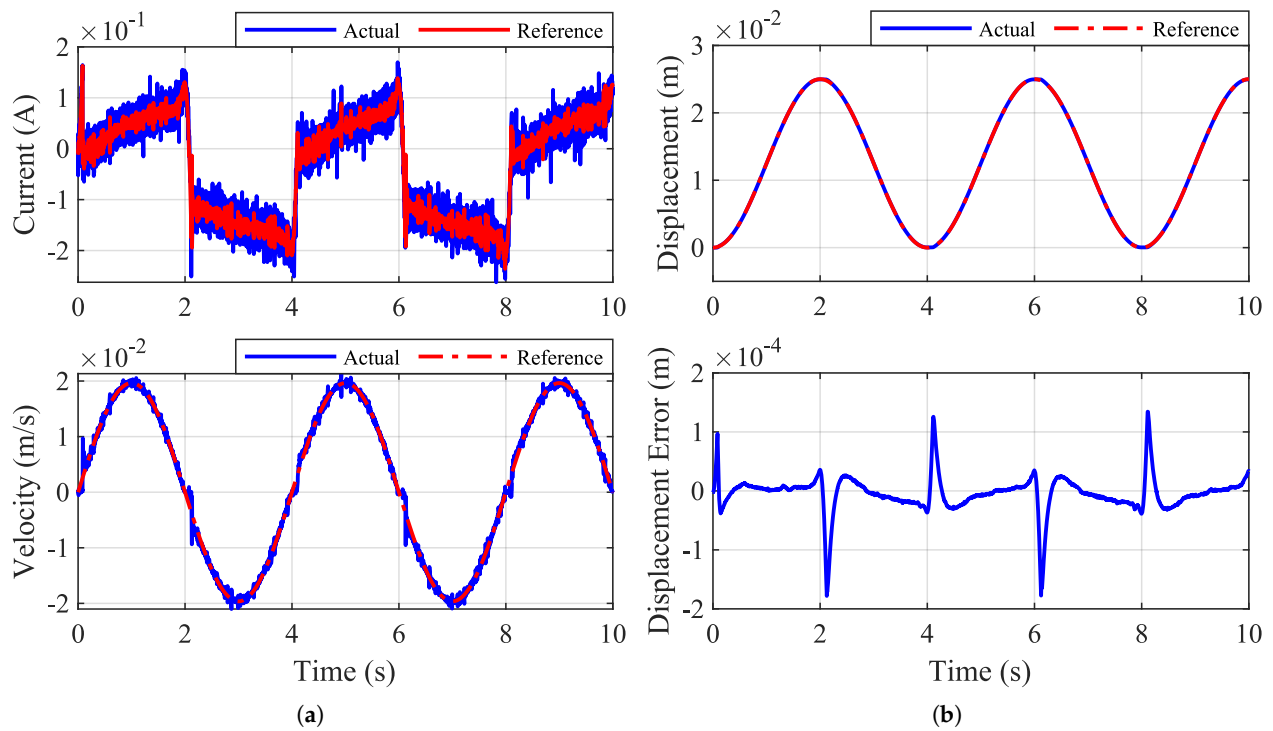


Figure 11. Experimental waveforms for sinusoidal position tracking at 0.25 Hz with $\alpha = 5$, $K_v = 20$, $K_p = 40$. (a) Current and velocity; (b) displacement and displacement error.

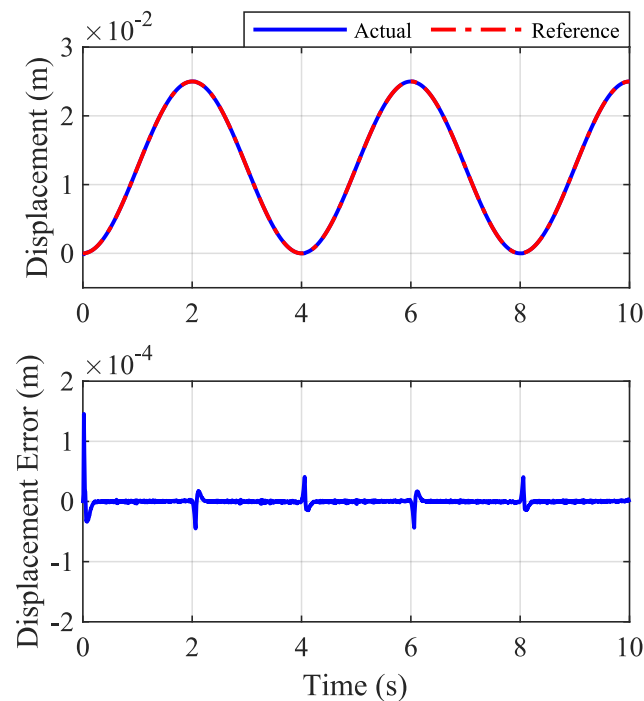


Figure 12. Experimental waveforms for sinusoidal position tracking at 0.25 Hz with $\alpha = 50$, $K_v = 20$, $K_p = 40$.

The effect of changing K_p is also studied. Figure 13 shows the zoomed view of the transient response for three sinusoidal position-tracking experiments at 0.5 Hz with $K_v = 20$ and $\alpha = 5$, and with $K_p = 10, 20$, and 40. It can be observed that as K_p is increased, the transient and settling time are reduced.

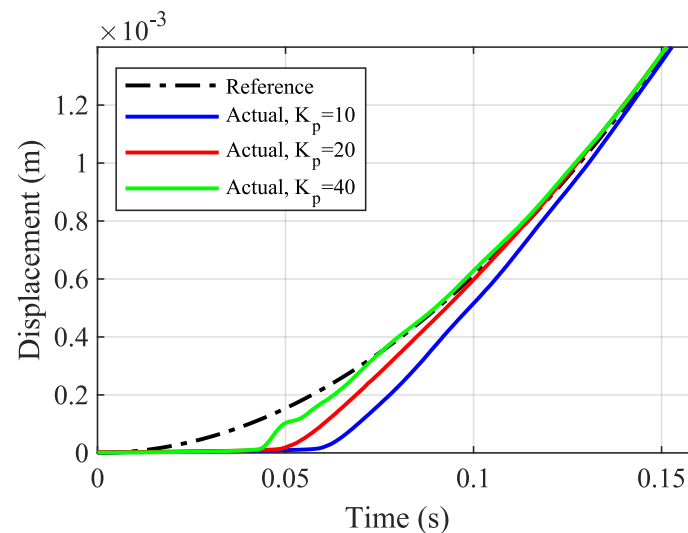


Figure 13. Zoomed view of the transient response for three sinusoidal position-tracking experiments at 0.25 Hz with $K_v = 20$ and $\alpha = 5$.

5.3. Comparative Analysis of STRC with ADRC

The sinusoidal tracker has been further tuned and compared with the ADRC method at three different frequencies with the same amplitude. The new STRC gains are $\alpha = 5$, $K_v = 39.2$, and $K_p = 100$, which still meet the design criteria presented in Section 3.1.

The ADRC parameters are selected using the design methodology presented in Section 4 and are given as follows: $w_c = 30$, $w_o = 150$, $\kappa = 9$, $\epsilon_1 = \epsilon_2 = 0.5$, $\eta_1 = \eta_2 = 0.1$, $\lambda_1 = 0.9$, $\lambda_2 = 0.25$, $\psi_1 = \psi_2 = 0.1$ and the sampling time $h_0 = 1$ ms.

Figures 14–16 show the motor speed, position reference, and actual position for three experimental tests comparing the STRC and the ADRC methods at $f_0 = 1.0$ Hz, 0.5 Hz, and 0.25 Hz, respectively. The root mean square error (RMSE) for each full period at these three frequencies is given in Table 4. It can be noticed that the RMSE at 1.0 Hz is an order of magnitude better than the ADRC for both the position and the velocity.

It can be observed in Figure 14 that there is a noticeable phase shift for the ADRC response. This phase shift is reduced as the frequency is reduced. At the lowest frequency, the position and the velocity RMSEs for the STRC are still lower than the ADRC RMSE values and with fewer oscillations around the zero-crossing region, as can be seen in Figure 16.

Table 4. Root mean square error for one full period at three different frequencies comparing STRC and ADRC methods.

Frequency	RMSE Position		RMSE Velocity	
	STRC	ADRC	STRC	ADRC
1.00 Hz	2.25×10^{-5}	3.48×10^{-4}	6.31×10^{-4}	2.53×10^{-3}
0.50 Hz	2.79×10^{-5}	6.90×10^{-5}	4.62×10^{-4}	1.00×10^{-3}
0.25 Hz	3.31×10^{-5}	4.51×10^{-5}	3.46×10^{-4}	5.30×10^{-4}

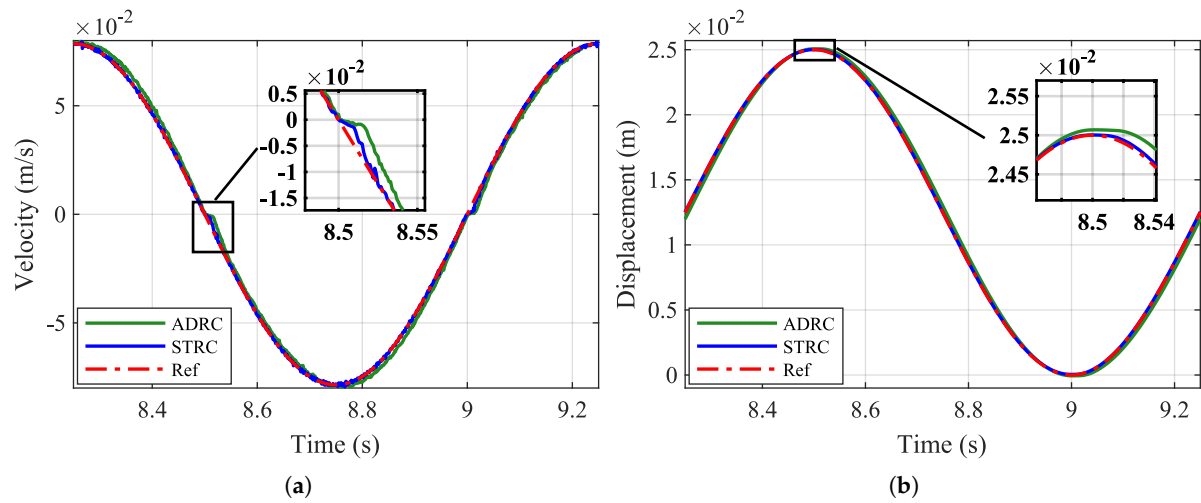


Figure 14. Experimental waveform comparison at 1.0 Hz. (a) Velocity; (b) displacement.

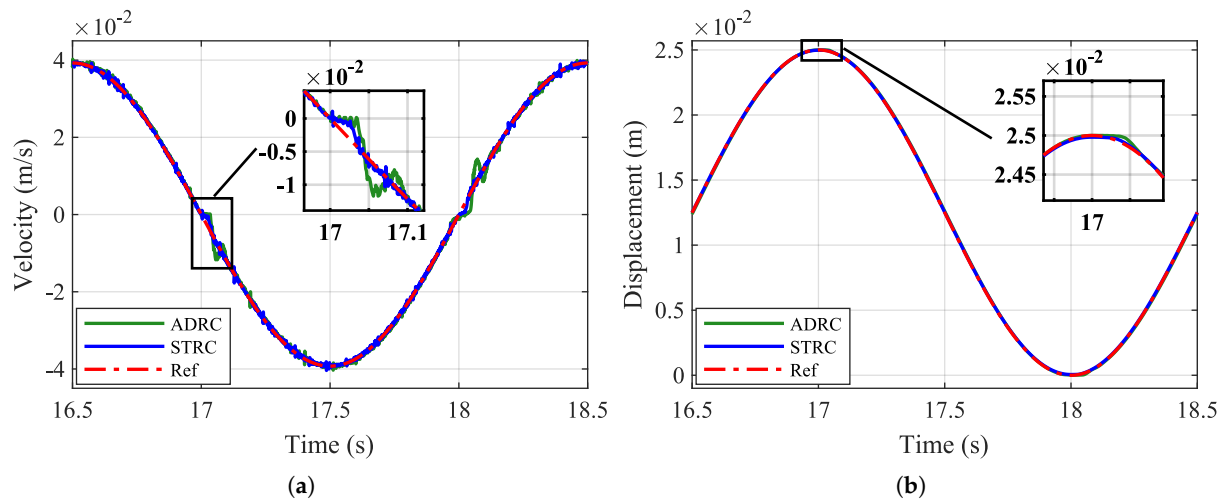


Figure 15. Experimental waveform comparison at 0.5 Hz. (a) Velocity; (b) displacement.

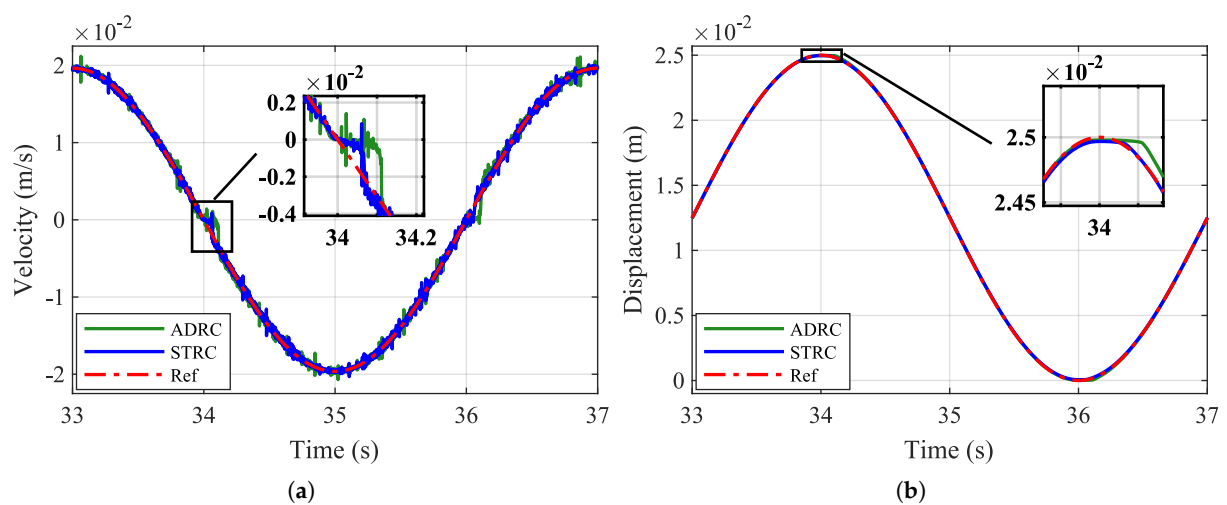


Figure 16. Experimental waveform comparison at 0.25 Hz. (a) Velocity; (b) displacement.

It can be observed that for different frequencies, the STRC tracking is excellent, with almost indistinguishable reference and output signals. It is also clear that the selection of the controller gains is flexible while achieving the desired tracking performance. Only approximate values of the nominal system parameters are needed to find the upper and lower bounds of the controller gains. This confirms that position-tracking errors are significantly decreased with the proposed STRC controller.

5.4. Response to System Parameters Variation

An extra mass of 100g has been added to the linear stage while it is moving, to compare the response of both controllers. This extra mass represents about 10% of the linear stage moving mass. Figures 17 and 18 show a comparison between the STRC and the ADRC methods at $f_0 = 0.25$ Hz, respectively, and using the same controllers' parameters listed in Section 5.3 when an extra mass is introduced to the system. For both controllers, two periods are captured. The first period shows the transient response error when the system starts from zero. In the second period, the extra mass is added to the moving stage, and it shows the system response reacting to this disturbance.

In this experiment, the reference position is chosen to have an amplitude of 35 mm rather than 25 mm, as in all previous experiments, to show the effect of adding the extra mass to the system. From Figures 17 and 18, it can be observed that the maximum absolute displacement error for the STRC method is about 0.6×10^{-4} m, while the ADRC method is about 2×10^{-4} m. This experiment shows that while both methods are effective at canceling the disturbance effect, the STRC is still superior in terms of tracking the reference input.

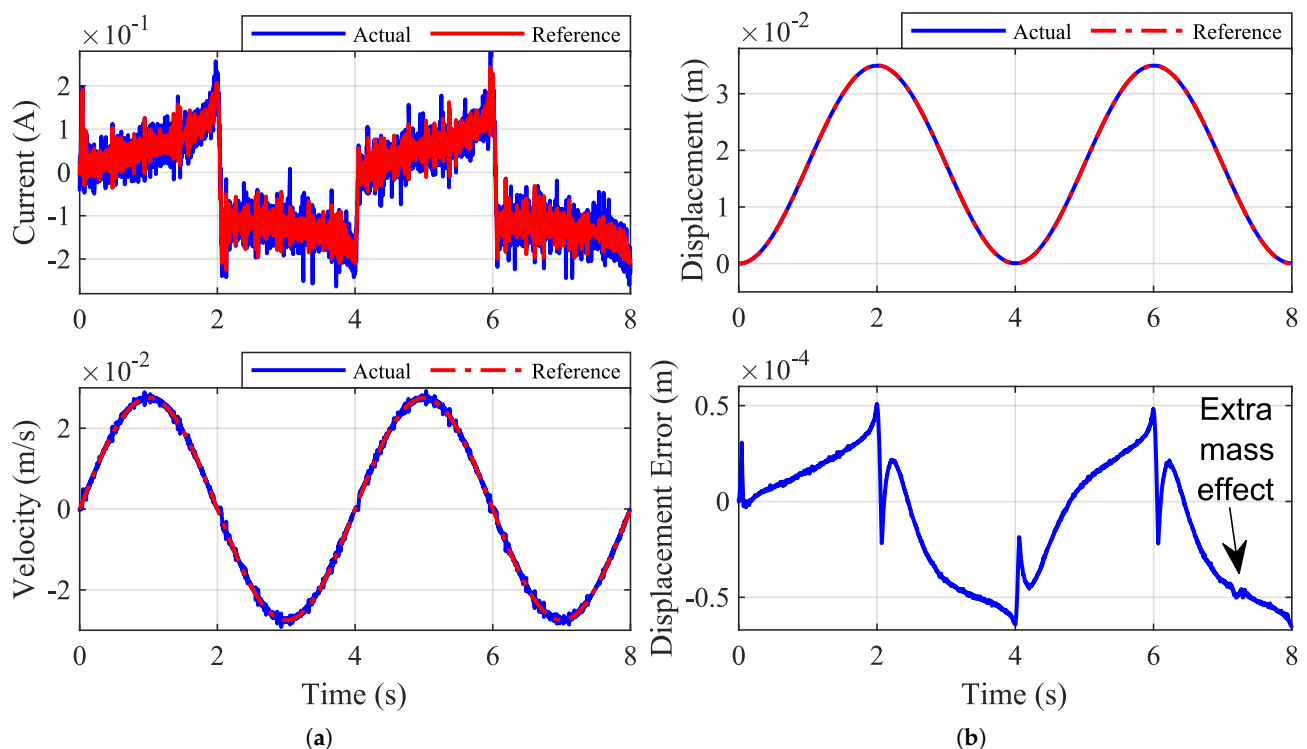


Figure 17. Experimental waveforms for sinusoidal position-tracking using the STRC method for two consecutive periods at 0.25 Hz showing the effect of extra mass when introduced in the second period. (a) Current and velocity; (b) displacement and displacement error.

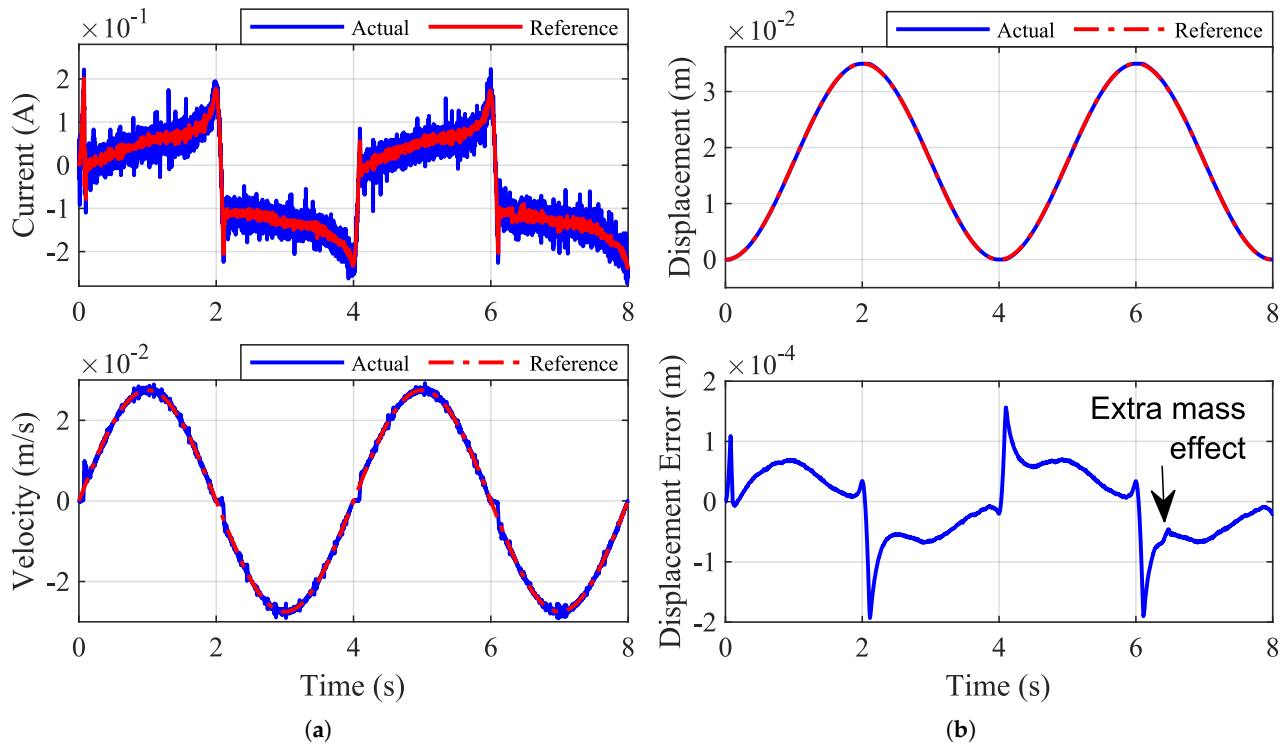


Figure 18. Experimental waveforms for sinusoidal position-tracking using the ADRC method for two consecutive periods at 0.25 Hz showing the effect of extra mass when introduced in the second period. (a) Current and velocity; (b) displacement and displacement error.

5.5. STRC Performance with Higher-Order Dynamics

The performance of the proposed STRC controller is further validated with a more complex system by adding high-order dynamics to the VCM linear stage. The motor assembly is assumed to include a flexible spacer between the slider and the load mass. This elastic coupling results in a two-mass model (2MM) structure with a spring constant k parallel to a viscous damping coefficient b , as shown in Figure 19.

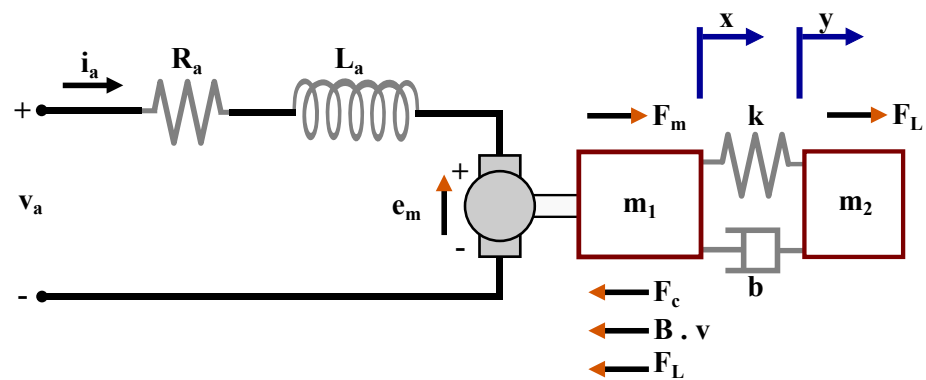


Figure 19. Two-mass model of a voice-coil DC motor.

The spring constant k can be found as follows:

$$k = \frac{m_1 m_2 \omega_n^2}{m_1 + m_2}, \quad (73)$$

where ω_n is the resonant frequency of the elastic system in (rad/s).

The STRC controller is designed in this case by replacing the 2MM system with the equivalent rigid system given in Figure 1, where $M = m_1 + m_2$. Without any tuning to the

STRC controller's parameters, the STRC gains which are used in Section 5.3 are used for this experiment, i.e., $\alpha = 5$, $K_v = 39.2$, and $K_p = 100$. The simulation results are obtained at a frequency of $f_0 = 0.25\text{ Hz}$ using Matlab/Simulink for the single mass model and the 2MM system with $m_1 = m_2 = 0.5$, $M = 0.4616\text{ kg}$, $k = 22,779\text{ N/m}$, $b = 10\text{ N.s/m}$, and $\omega_n = (2\pi \times 50)\text{ rad/s}$.

Figure 20 shows the hysteresis current-control signals for a simulation test comparing the STRC with the single mass and the STRC with the 2MM system. Figure 21 shows the motor speed and position signals for this simulation test. The root mean square error for a full period is given in Table 5.

It can be observed that STRC tracking is excellent regardless of whether the system is relatively simple or whether it includes higher-order dynamics. It can be noticed that the velocity RMSE for the STRC is still better than that for the 2MM at this frequency. This can be related to the higher oscillations in the reference current signal for the 2MM, as can be seen in Figure 20b. It should be noted that the gains are not fine-tuned for the 2MM and that a good performance can still be achieved. This shows the flexibility of choosing the controller gains while achieving the desired tracking performance. Only approximate values of the nominal system parameters are needed to find the upper and lower bounds of the controller gains.

Table 5. Root mean square error for one full period at a frequency of 0.25 Hz comparing STRC and STRC-2MM models.

Frequency	RMSE Position		RMSE Velocity	
	STRC	STRC-2MM	STRC	STRC-2MM
0.25 Hz	3.47×10^{-6}	3.50×10^{-6}	9.40×10^{-5}	1.23×10^{-4}

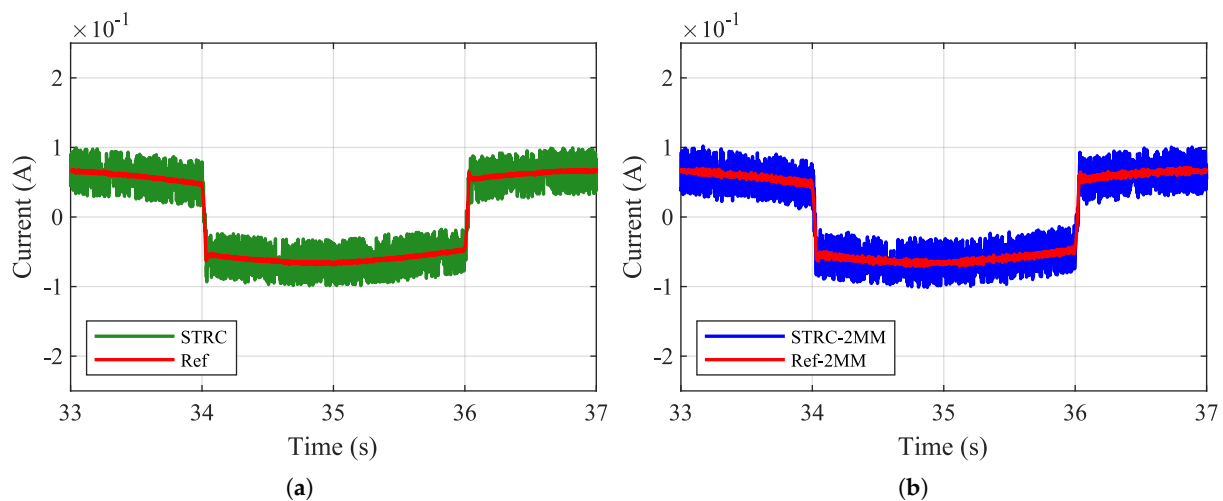


Figure 20. Simulation waveform comparison at 0.25 Hz. (a) STRC hysteresis current-control signals; (b) STRC-2MM hysteresis current-control signals.

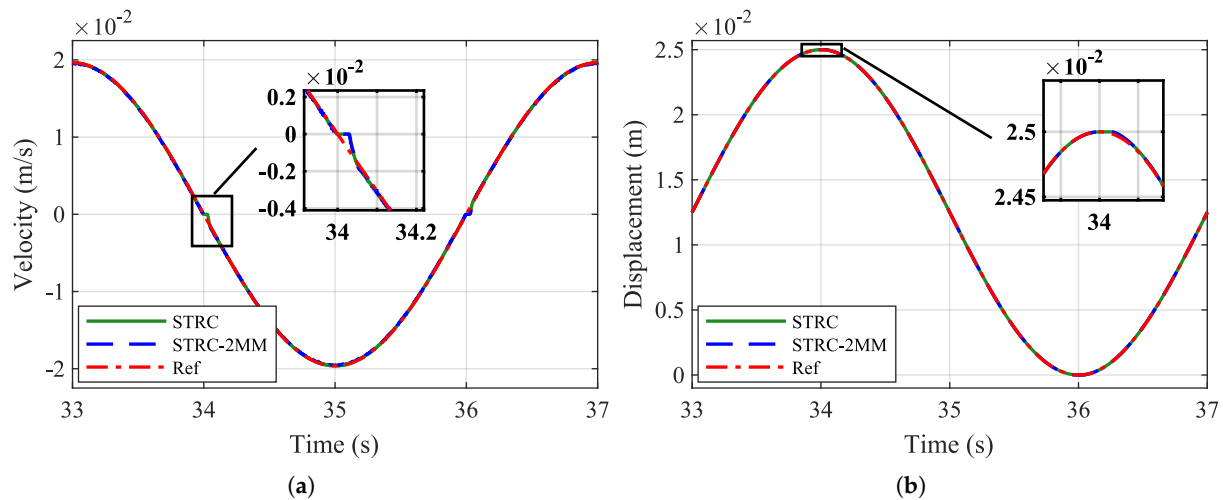


Figure 21. Simulation waveform comparison at 0.25 Hz. (a) Velocity; (b) displacement.

6. Conclusions

In this paper, we proposed a new sinusoidal position-tracking control scheme with a resonant controller for linear motor drive systems. The STRC controller is designed without any added algorithm for system identification and requires only approximate values of the mechanical parameters. Therefore, the controller is simple and robust in parameter variations. An optimal feedback principle and corresponding parameter-tuning based on the Routh–Hurwitz stability criterion are proposed, which are characterized by an ease of design and implementation. Nonlinear friction and external disturbance were successfully canceled by the proposed method. Experimental validations show that the proposed STRC strategy shows superior dynamic performance in terms of tracking speed and steady-state error at different frequencies with a maximum error of 0.58% at 0.25 Hz.

The proposed STRC controller is compared with the ADRC controller. The STRC method requires the tuning of only 3 parameters compared to 11 parameters for the ADRC method. Nevertheless, the STRC shows a huge performance improvement in terms of tracking speed and steady-state error at different frequencies when compared to the ADRC method. Even when an extra mass is introduced to the system, and while both methods are good in canceling the disturbance effect, the STRC is still superior in terms of tracking the reference input. The proposed STRC controller is further validated by simulating a more complex system which adds high-order dynamics to the VCM linear stage. Future work may include comparing the proposed STRC method with other state-of-the-art schemes.

Author Contributions: Conceptualization, R.D. and M.T.; methodology, R.D.; software, M.T. and I.H.; validation, R.D., M.T. and I.H.; formal analysis, R.D. and M.T.; investigation, M.T. and I.H.; resources, R.D., M.T. and I.H.; data curation, M.T. and I.H.; writing—original draft preparation, R.D. and M.T.; writing—review and editing, R.D. and M.T.; visualization, M.T.; supervision, R.D.; project administration, R.D.; funding acquisition, R.D. All authors have read and agreed to the published version of the manuscript.

Funding: This research was funded by the Petrofac Research Chair in Renewable Energy Endowment Fund, the American University of Sharjah, Sharjah, UAE.

Institutional Review Board Statement: Not applicable.

Informed Consent Statement: Not applicable.

Data Availability Statement: Not applicable.

Acknowledgments: This paper represents the opinions of the author(s) and does not mean to represent the position or opinions of the American University of Sharjah.

Conflicts of Interest: The authors declare no conflict of interest. The funders had no role in the design of the study; in the collection, analyses, or interpretation of data; in the writing of the manuscript; or in the decision to publish the results.

Abbreviations

The following abbreviations are used in this manuscript:

STRC	Sinusoidal Tracking Resonant-based Controller
VCA	Voice-Coil Actuator
VCM	Voice-Coil Motor
PID	Proportional–Integral–Derivative
ADRC	Adaptive Disturbance Rejection Control
EMF	Back Electromotive Force
TPG	Tracking Profile Generator
NWS	Nonlinear Weighted Sum
ESO	Extended State Observer
RMSE	Root Mean Square Error
2MM	Two Mass Model

References

1. Zheng, J.; Fu, M.; Lu, R.; Xie, S. Design, Identification, and Control of a Linear Dual-Stage Actuation Positioning System. *J. Frankl. Inst.* **2018**, *355*, 5018–5036. [\[CrossRef\]](#)
2. Huang, D.; Venkataramanan, V.; Xu, J.X.; Huynh, T.C.T. Contact-Induced Vibration in Dual-Stage Hard Disk Drive Servo Systems and Its Compensator Design. *IEEE Trans. Ind. Electron.* **2014**, *61*, 4052–4060. [\[CrossRef\]](#)
3. Landolsi, T.; Dhaouadi, R.; Aldabbas, O. Beam-Stabilized Optical Switch Using a Voice-Coil Motor Actuator. *J. Frankl. Inst.* **2011**, *348*, 1–11. [\[CrossRef\]](#)
4. Smith, K.J.; Graham, D.J.; Neasham, J.A. Design and Optimization of a Voice Coil Motor with a Rotary Actuator for an Ultrasound Scanner. *IEEE Trans. Ind. Electron.* **2015**, *62*, 7073–7078. [\[CrossRef\]](#)
5. Ryoo, J.R.; Jin, K.B.; Moon, J.H.; Chung, M.J. Track-Following Control Using a Disturbance Observer with Asymptotic Disturbance Rejection in High-Speed Optical Disk Drives. *IEEE Trans. Consum. Electron.* **2003**, *49*, 1178–1185. [\[CrossRef\]](#)
6. Shinshi, T.; Shimizu, D.; Kodeki, K.; Fukushima, K. A Fast Steering Mirror Using a Compact Magnetic Suspension and Voice Coil Motors for Observation Satellites. *Electronics* **2020**, *9*, 1997. [\[CrossRef\]](#)
7. Shen, C.; Chen, N.; Tan, R.; Fan, S.; Fan, D. Modeling and Stability Analysis of Coarse–Fine Composite Mechatronic System in UAV Multi-Gimbal Electro-Optical Pod. *Electronics* **2020**, *9*, 769. [\[CrossRef\]](#)
8. Liu, C.S.; Wu, Y.C.; Lan, Y.J. Design of 4-DOF Voice Coil Motor with Function of Reducing Laser Geometrical Fluctuations. *Actuators* **2021**, *10*, 320. [\[CrossRef\]](#)
9. Lin, Y.H.; Liu, C.S.; Yeh, C.N. Design and Simulation of Novel 3-DOF Spherical Voice Coil Motor. *Actuators* **2021**, *10*, 155. [\[CrossRef\]](#)
10. Armstrong-Helouvry, B.; Dupont, P.; Canudasdewit, C. Survey of Models, Analysis Tools and Compensation Methods for the Control of Machines with Friction. *Automatica* **1994**, *30*, 1083–1138. [\[CrossRef\]](#)
11. Tan, K.; Huang, S.; Lee, T. Robust Adaptive Numerical Compensation for Friction and Force Ripple in Permanent-Magnet Linear Motors. *IEEE Trans. Magn.* **2002**, *38*, 221–228. [\[CrossRef\]](#)
12. Lin, C.J.; Yau, H.T.; Tian, Y.C. Identification and Compensation of Nonlinear Friction Characteristics and Precision Control for a Linear Motor Stage. *IEEE/ASME Trans. Mechatron.* **2013**, *18*, 1385–1396. [\[CrossRef\]](#)
13. Verbert, K.A.J.; Tóth, R.; Babuška, R. Adaptive Friction Compensation: A Globally Stable Approach. *IEEE/ASME Trans. Mechatron.* **2016**, *21*, 351–363. [\[CrossRef\]](#)
14. Nie, K.; Xue, W.; Zhang, C.; Mao, Y. Disturbance Observer-Based Repetitive Control with Application to Optoelectronic Precision Positioning System. *J. Frankl. Inst.* **2021**, *358*, 8443–8469. [\[CrossRef\]](#)
15. Lan, Y.H.; He, J.L.; Li, P.; She, J.H. Optimal Preview Repetitive Control with Application to Permanent Magnet Synchronous Motor Drive System. *J. Frankl. Inst.* **2020**, *357*, 10194–10210. [\[CrossRef\]](#)
16. Kerschen, G.; Worden, K.; Vakakis, A.F.; Golinval, J.C. Past, Present and Future of Nonlinear System Identification in Structural Dynamics. *Mech. Syst. Signal Process.* **2006**, *20*, 505–592. [\[CrossRef\]](#)
17. Ljung, L. *Identification of Nonlinear Systems*; Other academic LiTH-ISY-R, 2784; Department of Electrical Engineering, Linköping University: Linköping, Sweden, 2007.
18. Waleed, D.; Usman, H.M.; Dhaouadi, R. Dynamic Friction Characterization of a Linear Servo Motor Using an Optimal Sinusoidal Reference Tracking Controller. *J. Robot. Mechatronics* **2018**, *30*, 1014–1018. [\[CrossRef\]](#)
19. Noorbakhsh, M.; Yazdizadeh, A. Adaptive Friction Compensation in a Two-Link Planar Robot Manipulator Using a New Lyapunov-Based Controller. In Proceedings of the IEEE ICCA 2010, Xiamen, China, 9–11 June 2010; pp. 2132–2137. [\[CrossRef\]](#)

20. Ryu, J.H.; Song, J.; Kwon, D.S. A Nonlinear Friction Compensation Method Using Adaptive Control and its Practical Application to an In-Parallel Actuated 6-DOF Manipulator. *Control. Eng. Pract.* **2001**, *9*, 159–167. [\[CrossRef\]](#)
21. Kim, W.; Shin, D.; Won, D.; Chung, C.C. Disturbance-Observer-Based Position Tracking Controller in the Presence of Biased Sinusoidal Disturbance for Electrohydraulic Actuators. *IEEE Trans. Control. Syst. Technol.* **2013**, *21*, 2290–2298. [\[CrossRef\]](#)
22. Wang, Z.; Wang, H.; Li, Y.; Blaabjerg, F. A Single Position Loop Control Strategy for High-Speed Voice Coil Motor Based on Active Disturbance Rejection Control. In Proceedings of the 2017 IEEE 26th International Symposium on Industrial Electronics (ISIE), Edinburgh, UK, 19–21 June 2017; pp. 220–225. [\[CrossRef\]](#)
23. Gao, Y. Active Disturbance-Rejection Control of Voice Coil Motor Based on RBF Neural Network. In Proceedings of the 2011 International Conference on Consumer Electronics, Communications and Networks (CECNet), Xianning, China, 16–18 April 2011; pp. 3895–3898. [\[CrossRef\]](#)
24. Gao, Z. Scaling and Bandwidth-Parameterization Based Controller Tuning. In Proceedings of the 2003 American Control Conference, Denver, CO, USA, 4–6 June 2003; Volume 6, pp. 4989–4996. [\[CrossRef\]](#)
25. Chen, Q.; Li, L.; Wang, M.; Pei, L. The Precise Modeling and Active Disturbance Rejection Control of Voice Coil Motor in High Precision Motion Control System. *Appl. Math. Model.* **2015**, *39*, 5936–5948. [\[CrossRef\]](#)
26. Chatterjee, A.; Mohanty, K.B. Current Control Strategies for Single Phase Grid Integrated Inverters for Photovoltaic Applications—A Review. *Renew. Sustain. Energy Rev.* **2018**, *92*, 554–569. [\[CrossRef\]](#)
27. Ming, L.; Xin, Z.; Kong, X.; Yin, C.; Loh, P.C. Power Factor Correction and Harmonic Elimination for LCL-Filtered Three-Level Photovoltaic Inverter with Inverter-Side Current Control. In Proceedings of the IECON 2019—45th Annual Conference of the IEEE Industrial Electronics Society, Lisbon, Portugal, 14–17 October 2019; Volume 1, pp. 3405–3410. [\[CrossRef\]](#)
28. Santiprapan, P.; Areerak, K.; Areerak, K. The Implementation of Active Power Filter using Proportional plus Resonant Controller. *Eng. J.* **2017**, *21*, 69–80. [\[CrossRef\]](#)
29. Xu, Q.; Jia, M. Model Reference Adaptive Control with Perturbation Estimation for a Micropositioning System. *IEEE Trans. Control. Syst. Technol.* **2014**, *22*, 352–359. [\[CrossRef\]](#)
30. Esbrook, A.; Guibord, M.; Tan, X.; Khalil, H.K. Control of Systems with Hysteresis via Servocompensation and its Application to Nanopositioning. In Proceedings of the 2010 American Control Conference, Baltimore, MD, USA, 30 June–2 July 2010; pp. 6531–6536. [\[CrossRef\]](#)
31. Yepes, A.G.; Freijedo, F.D.; Doval-Gandoy, J.; Lopez, O.; Malvar, J.; Fernandez-Comesaña, P. Effects of Discretization Methods on the Performance of Resonant Controllers. *IEEE Trans. Power Electron.* **2010**, *25*, 1692–1712. [\[CrossRef\]](#)
32. Nian, H.; Wu, C.; Cheng, P. Direct Resonant Control Strategy for Torque Ripple Mitigation of DFIG Connected to DC Link through Diode Rectifier on Stator. *IEEE Trans. Power Electron.* **2017**, *32*, 6936–6945. [\[CrossRef\]](#)
33. Wang, X.; Sun, D.; Zhu, Z.Q. Resonant Based Backstepping Direct Power Control Strategy for DFIG Under Both Balanced and Unbalanced Grid Conditions. In Proceedings of the IEEE Energy Conversion Congress and Exposition (ECCE), Milwaukee, WI, USA, 18–22 September 2016; pp. 1–8. [\[CrossRef\]](#)
34. Touati, Z.; Pereira, M.; Araújo, R.E.; Khedher, A. Comparative Study of Discrete PI and PR Controller Implemented in SRG for Wind Energy Application: Theory and Experimentation. *Electronics* **2022**, *11*, 1285. [\[CrossRef\]](#)
35. Cordero, R.; Estrabis, T.; Brito, M.A.; Gentil, G. Development of a Resonant Generalized Predictive Controller for Sinusoidal Reference Tracking. *IEEE Trans. Circuits Syst. II Express Briefs* **2022**, *69*, 1218–1222. [\[CrossRef\]](#)
36. Zhou, Z.; Xia, C.; Yan, Y.; Wang, Z.; Shi, T. Disturbances Attenuation of Permanent Magnet Synchronous Motor Drives Using Cascaded Predictive-Integral-Resonant Controllers. *IEEE Trans. Power Electron.* **2018**, *33*, 1514–1527. [\[CrossRef\]](#)
37. Turner, M.C.; Sofrony, J.; Prempain, E. Anti-windup for model-reference adaptive control schemes with rate-limits. *Syst. Control. Lett.* **2020**, *137*, 104630. [\[CrossRef\]](#)
38. Hosseinzadeh, M.; Yazdanpanah, M.J. Performance enhanced model reference adaptive control through switching non-quadratic Lyapunov functions. *Syst. Control. Lett.* **2015**, *76*, 47–55. [\[CrossRef\]](#)
39. Kahani, R.; Jamil, M.; Iqbal, M.T. Direct Model Reference Adaptive Control of a Boost Converter for Voltage Regulation in Microgrids. *Energies* **2022**, *15*, 5080. [\[CrossRef\]](#)
40. Takrouiri, M.; Dhaouadi, R. ADALINE-based friction identification of a linear voice coil DC motor. In Proceedings of the 2016 American Control Conference (ACC), Boston, MA, USA, 6–8 July 2016; pp. 3062–3068. [\[CrossRef\]](#)
41. Dorf, R.C.; Bishop, R.H. *Modern Control Systems*, 13th ed.; Pearson: Hoboken, NJ, USA, 2017.
42. Al Kalbani, F.K.; Zhang, J. Inferential Active Disturbance Rejection Control of a Heat Integrated Distillation Column. In Proceedings of the 2016 14th International Conference on Control, Automation, Robotics and Vision (ICARCV), Phuket, Thailand, 13–15 November 2016; pp. 1–6. [\[CrossRef\]](#)
43. Han, J. From PID to Active Disturbance Rejection Control. *IEEE Trans. Ind. Electron.* **2009**, *56*, 900–906. [\[CrossRef\]](#)
44. Gao, Z. From Linear to Nonlinear Control Means: A Practical Progression. *ISA Trans.* **2002**, *41*, 177–189. [\[CrossRef\]](#) [\[PubMed\]](#)
45. Moticont. Linear Voice Coil Motors. 2023. Available online: <http://moticont.com/voice-coil-motor.htm> (accessed on 3 January 2023).

Disclaimer/Publisher’s Note: The statements, opinions and data contained in all publications are solely those of the individual author(s) and contributor(s) and not of MDPI and/or the editor(s). MDPI and/or the editor(s) disclaim responsibility for any injury to people or property resulting from any ideas, methods, instructions or products referred to in the content.